PCCP

Accepted Manuscript

ROYAL SOCIETY OF CHEMISTRY

www.rsc.org/pccp

Journal Name

ARTICLE TYPE

Cite this: DOI: 10.1039/xxxxxxxxxx

Mechanical Properties of Monolayer Sulphides: A Comparative Study between MoS_2, HfS_2 and TiS_3

Jun Kang,* Hasan Sahin,* and François M. Peeters*

Received Date
Accepted Date

DOI: 10.1039/xxxxxxxxxx

www.rsc.org/journalname

The in-plane stiffness (C), Poisson's ratio (ν), Young's modulus and ultimate strength (σ) along two different crystallographic orientations are calculated for the single layer crystals: MoS_2, HfS_2 and TiS_3 in 1H, 1T and monoclinic phases. We find that MoS_2 and HfS_2 have isotropic in-plane stiffness of 124.24 N/m and 79.86 N/m, respectively. While for TiS_3 the in-plane stiffness are highly anisotropic due to its monoclinic structure, with C_x=83.33 N/m and C_y=133.56 N/m (x and y are parallel to its longer and shorter in-plane lattice vectors.). HfS_2 which is in the 1T phase has the smallest anisotropy in its ultimate strength, whereas TiS_3 in the monoclinic phase has the largest. Along the armchair direction MoS_2 has the largest σ of 23.48 GPa, whereas along y TiS_3 has the largest σ of 18.32 GPa. We have further analyzed the band gap response of these materials under uniaxial tensile strain, and find that they exhibit different behavior. Along both armchair and zigzag directions, the band gap of MoS_2 (HfS_2) decreases (increases) as strain increases, and the response is almost isotropic. For TiS_3, the band gap decreases when strain is along x, While if strain is along y, the band gap increases first and then decreases beyond a threshold strain value. The different characteristics observed in these sulphides with different structures shed light on the relationship between structure and properties, which are useful for applications in nanotechnology.

1 Introduction

The high mechanical strength and electronic quality of transition metal sulphides (TMSs) have attracted a lot of interest together with the chemical and physical properties of these materials.[1–4] Most of the TMSs form layered compounds where the closely-packed layers are held together by weak van der Waals forces. Ultra-thin TMSs have recently emerged as promising materials for new nanoscale devices in a wide variety of applications.[5,6] In these device applications, especially the semiconducting nature of ultra-thin sulphides make them superior to graphene, which is a semimetal. The chemical versatility of ultra-thin TMSs is another reason of the growing interest for these materials.[7]

The first synthesized member of ultra-thin TMSs was MoS_2. By using the micro-mechanical cleavage method, successful synthesis of single layer MoS_2 was achieved by Novoselov et al.[8] Shortly after this study, optical spectroscopy measurements on the number of layer dependent properties of MoS_2 revealed that the effect of quantum confinement leads to a crossover from an indirect gap to a direct-gap material in the limit of a single monolayer.[9] Significant enhancement in luminescence quantum efficiency of the single layer structure attracted further interest for this class of materials. Furthermore, experiments on the stiffness and breaking strength of monolayer MoS_2 showed that its mechanical strength is comparable to that of steel.[10] These findings on MoS_2 triggered efforts to use TMSs in flexible electronic nanodevice applications.

Following MoS_2, several new elements of TMSs emerged such as WS_2, VS_2, HfS_2 and TiS_3. It was shown by several groups that sulphides of Mo and W have similar properties such as lattice parameter and electronic structure[11–13] Although, some findings on the high moisture responsiveness of ultra-thin VS_2 were reported,[14] the literature on the evidence of stable single layers of this material is sparse. In addition, dimensionality dependent electronic properties of HfS_2, from bulk to single layer, was reported.[15] Differing from single layers of MoS_2, WS_2 and VS_2 which are in the 1H phase where the metal atom have trigonal prismatic coordination, single layer HfS_2 forms an octahedral phase (1T) in its ground state. In addition, recent experiments reported the successful synthesis of single layer TiS_3 which has an entirely different crystal symmetry.[16] It was shown that TiS_3 layers, which were isolated by viscoelastic mechanical exfoliation, have a high photoresponsivity and therefore they are promising materials for nanoscale transistors and optoelectronic devices.

In this work we investigate the mechanical properties of single layer TMSs: TiS_3, HfS_2 and MoS_2. Although the mechani-

Department of Physics, University of Antwerp, Groenenborgerlaan 171, B-2020 Antwerpen, Belgium; E-mail: jun.kang@uantwerpen.be; hasan.sahin@uantwerpen.be; francois.peeters@uantwerpen.be

cal response of MoS_2 has been well-studied experimentally and theoretically[39,42–45], the recently emerged structures TiS_3 and HfS_2 have not been investigated before. While our calculations on MoS_2 allow us to examine the reliability of the computational methodology, its results will be contrasted with those for TiS_3 and HfS_2, which have very different crystal structures.

The paper is organized as follows. Our computational approach is given in Sec. II. Ground state structural and electronic properties of TiS_3, HfS_2 and MoS_2 are discussed in Sec. III together with their vibrational properties. Our results on the elastic parameters, the ultimate strength and the strain dependent electronic structure are presented in Sec. IV. Our conclusions are presented in Sec. V.

2 Computational Methodology

The calculations are performed using the frozen-core projector augmented wave method[25] as implemented in the Vienna *ab initio* simulation package (VASP)[23,24]. The generalized gradient approximation of Perdew-Burke-Ernzerhof (GGA-PBE)[26] is chosen as exchange-correlation functional. In part of the calculations the Heyd-Scuseria-Ernzerhof (HSE06) hybrid functional[27,28] is also used to get better band gap values. Energy cutoff for plane-wave expansion is set to 400 eV. Brillouin zone sampling is performed with the Monkhorst-Pack (MP) special k-point meshes[29] including the Γ-point. For MoS_2 and HfS_2 a grid of $12\times12\times1$ is used, and for TiS_3 a grid of $7\times11\times1$ is used. A vacuum layer larger than 10 Å is added to avoid interaction between adjacent images. All atoms are allowed to relax until the calculated Hellmann-Feynman force on each atom is smaller than 0.01 eV/Å.

To ensure dynamical stability and to analyze Raman fingerprints of the single layer crystal structures: MoS_2, HfS_2 and TiS_3, we also calculate the phonon frequencies throughout the whole Brillouin zone using the Small Displacement Methodology with the forces obtained from VASP.[30]

3 Ground State Properties of TiS_3, HfS_2 and MoS_2

Before we give a comprehensive analysis of the mechanical properties of single layer TMSs, we will first briefly discuss their ground state properties. Since its first successful synthesis[8], electronic and vibrational properties of single layer MoS_2 have been studied by many groups. In the following, we examine the reliability of our computational methodology by comparing our results on MoS_2 with published results. Therefore we will present our results on the novel single layer crystal structures of TiS_3 and HfS_2.

While bulk MoS_2 (2H phase) belongs to the centrosymmetric D_{6h} point group, in the single layer structure (1H phase) the trigonal prismatic coordination of S atoms around the Mo atoms results in D_{3h} symmetry. Among the few-layered structures, even-number-of-layers have inversion symmetry, and belong to D_{6h} symmetry while for odd-number-of-layers (no inversion symmetry), they belong to D_{3h}. Therefore, one can expect some interesting thickness-dependent properties in the optoelectronic response of such structures.[36] In contrast to bulk MoS_2, HfS_2 is in the 1T

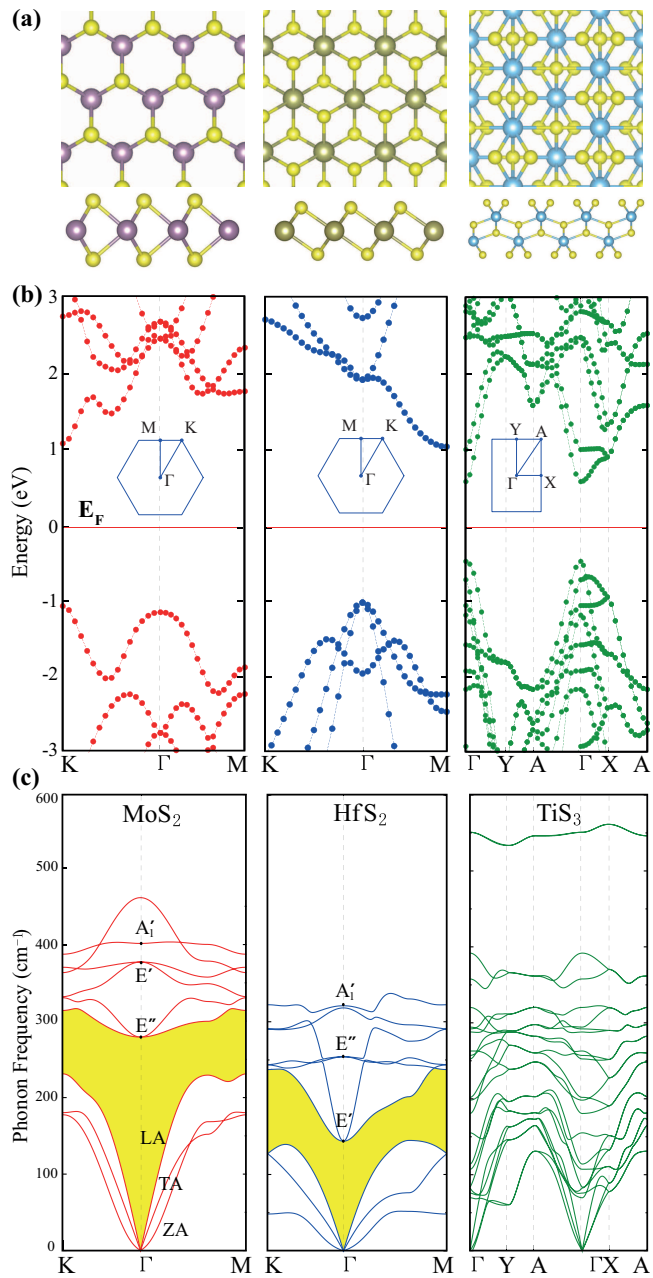

Fig. 1 (color online) (a) Out-of-plane view and side view of the single layer crystal structures of MoS_2, HfS_2 and TiS_3, (b) Electronic band dispersion obtained by performing DFT calculations with HSE06 functional and (c) Phonon dispersions. The gap between acoustical and optical phonon bands is highlighted with yellow color.

Table 1 Calculated lattice constants, the PBE and HSE06 energy bandgap of the structure, in-plane stiffness C and Young's modulus Y along x and y directions, Poisson's ratio (ν_i) and ultimate strength (σ_i) for single layer crystal structures of MoS_2, HfS_2 and TiS_3.

	structure	lattice constant (Å)	E_g^{PBE} (eV)	E_g^{HSE06} (eV)	C_x (N/m)	C_y (N/m)	Y_x (GPa)	Y_y (GPa)	ν_x	ν_y	σ_x (GPa)	σ_y (GPa)
MoS_2	1H	3.18	1.68	2.14	124.24	124.24	202.18	202.18	0.25	0.25	23.48	15.99
HfS_2	1T	3.64	1.28	2.06	79.86	79.86	136.82	136.82	0.19	0.19	14.16	12.38
TiS_3	monoclinic	5.02, 3.41	0.25	1.05	83.33	133.56	95.72	153.41	0.11	0.18	4.45	18.32

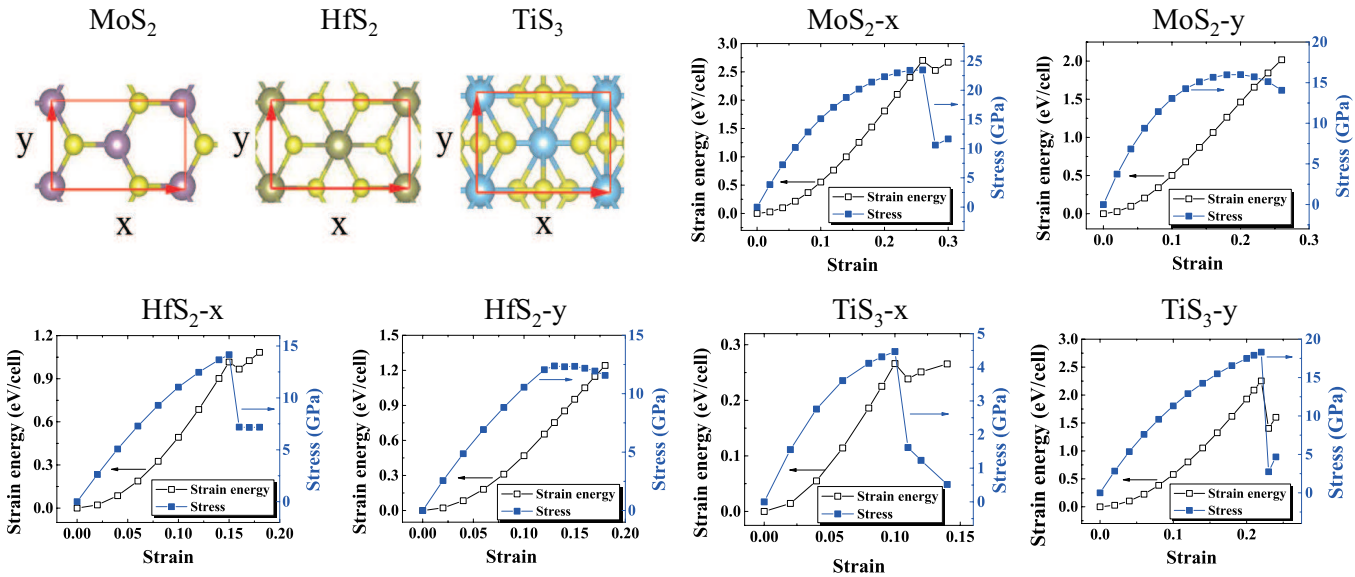

Fig. 2 (color online) The variation of strain energy and stress with uniaxial strain along x and y directions for MoS_2, HfS_2 and TiS_3. Rectangular unit cells used in the calculations are also shown in the top left panels.

phase with an inversion center at the Hf atom sites. Therefore both bulk and monolayers of HfS_2 belong to the D_{3d} point group. In addition, recent studies showed that similar to MoS_2 and HfS_2, layers of TiS_3 are held together by weak van der Waals forces and single layers can be exfoliated from their bulk structure.[16,17] As shown in Fig. 1(a), TiS_3 forms a monoclinic crystal structure. Here each monolayer is composed of interconnected chains of triangular TiS_3 prisms. In Table 1, we list the basic properties of the three sulphides. The optimized lattice constant for MoS_2 and HfS_2 are 3.18 Å and 3.64 Å, respectively. TiS_3 has two different lattice constants within the layer plane. The calculated values are 5.02 Å and 3.41 Å, close to the corresponding bulk values (4.96 Å and 3.40 Å).[38] Other study also predicted similar results (5.00 Å and 3.39 Å) for TiS_3 monolayers.[41] To further explore the chemical bonding characters we performed a Bader charge analysis. It is seen that the charge transfer per S atom for MoS_2 and HfS_2 are -0.5 e and -1.0 e, respectively. Therefore, the bonds in HfS_2 are more ionic than in MoS_2. However, for TiS_3, there are two different types of S atoms. The S atoms on the surface receive 0.3 e/atom from Ti, whereas the S atoms in the interior receive 0.8 e/atom, due to their larger coordination number.

From the electronic band dispersions, shown in Fig. 1(b), we find that these monolayer crystals are not only structurally different but display also electronically different characteristics. While monolayer MoS_2 is a direct bandgap semiconductor where valence and conduction band edges are located at the K point, HfS_2 displays an indirect bandgap (valence band maximum (VBM) is at the Γ-point and the conduction band minima (CBM) is at the M-point). However, TiS_3 is a direct bandgap material where the band edges are at the Γ-point. The HSE06 predicted band gaps for MoS_2, HfS_2 and TiS_3 are 2.14 eV, 2.06 eV and 1.05 eV, respectively. We found that the energy dispersions of the bands calculated by HSE06 and PBE were similar, except for the band gap values. Therefore, in the following our discussions will be based on the computationally less expensive PBE results.

The phonon dispersion of monolayer MoS_2, HfS_2 and TiS_3 are shown in Fig. 1(c). In addition to energy optimization calculations, real phonon eigenfrequencies are another indication of the dynamical stability of these single layer crystals. The phonon property of MoS_2 was well studied in many papers[31,35], and our phonon dispersion in Fig. 1(c) is quite similar to the reported ones. While there is a gap between optical and acoustic phonon branches in MoS_2 and HfS_2, those phonon branches are mixed in TiS_3. We also see that due to the larger atomic radius of the Hf atom and the relative weaker chemical bonding in HfS_2, the phonon modes are softer in this crystal. Although the acoustic modes of MoS_2 and HfS_2 have almost the same dispersion around the zone center, the flexural mode (ZA) shows qualitative different behavior at the zone boundaries K and M. It is also seen that differing from MoS_2 and HfS_2 the ZA of TiS_3 has almost a linear dispersion. In other works such linear dispersion was also observed[41]. The ZA mode corresponds to the vibration along the out-of-plane direction. The quadratic dispersion of ZA mode is a typical feature of many 2D materials[32,33,35], but for bulk-like structure it is linear. The observed deviation from the quadratic behavior is due to the multi-layered bulk-like structure of TiS_3. In a single layer TiS_3, there are six atomic layers (two Ti-layers and four S-layers). Each Ti-layer bonds to three S-layers. On the other hand, in single layers of MoS_2 and Hf_2, there are only three atomic layers (one metal-atom-layer bonded to two S-layers). Therefore, TiS_3 has much more bonds which connect different atom-layers than MoS_2 and Hf_2 have. In other words, TiS_3 is vibrationally much more bulk-like along the out-of-plane direction than many other 2D materials as MoS_2 and HfS_2, which results in the linear phonon dispersion around the Γ point. Analysis of the decomposition of the vibration representation of the optical modes at the Γ point reveal that both MoS_2 and HfS_2 can be characterized with the vibration representation $\Gamma = 2E'' + 2E' + A_1' + A_2''$. As highlighted in Fig. 1(c), among these modes only E'' (E_{1g} in bulk), E' (E_{2g} in bulk) and A_1' (A_g in bulk) modes are Raman active. The Raman active modes of MoS_2 are 279 cm^{-1} (E″), 377 cm^{-1} (E′) and 401 cm^{-1} (A_1') which compare with 289 cm^{-1}, 392 cm^{-1} and 410 cm^{-1} as found theoretically in Ref.[35]. The good agreement indicates that our computational method is reliable. However, for TiS_3, decomposition of the modes at the zone center is $\Gamma = 8A_g + 4B_g + 4A_u + 8B_u$. For the A_g and B_u modes, the motion of the atoms is perpendicular to the shorter in-plane lattice vector, while for the A_u and B_g modes the motion is parallel to it. On the other hand, the upper and lower TiS_3 units within the unit cell have counter-phase motion for A_g and B_g modes but in-phase motion for A_u and B_u modes. The A_g and B_g modes are Raman-active, and several modes at 559 (A_g), 371 (A_g), 300 (A_g), 176 (A_g), 102 (B_g) cm^{-1} have already been reported experimentally before for bulk TiS_3.[34] Our calculated values for these modes are 551, 358, 294, 155 and 107 cm^{-1}, in good agreement with the experimental results. In addition, the highest optical mode (around 550 cm^{-1}) which is well-separated in TiS_3 is another indication of its structural difference from MoS_2 and HfS_2.

4 Mechanical Response of TiS_3, HfS_2 and MoS_2

4.1 Elastic parameters

In-plane stiffness and Poisson's ratio are two important elastic parameters that characterize the mechanical response of 2D crystal structures. The in-plane stiffness C, which is a measure of the rigidity of a crystal structure, is defined as $C = (1/S_0)(\partial^2 E_s/\partial\varepsilon^2)$, where S_0 is the equilibrium area of the 2D material, E_s is the strain energy (the energy difference between the equilibrium and the strained structure) and ε is the applied strain. For a 2D crystal the larger C the less the stretchability.

Poisson's ratio ν, which is a measure of the lattice expansion of the crystal when compressed in a certain direction, is given by the formula $\nu = -\varepsilon_{\text{trans}}/\varepsilon_{\text{axial}}$. C and ν can be obtained through calculating the strain-energy relationship, as described in Ref.[18]. First, we construct rectangular unit cells of MoS_2, TiS_3 and HfS_2, as shown in Fig. 2. With this choice, two lattice vectors are directed along the x and y directions. For hexagonal MoS_2 and HfS_2, x and y correspond to the armchair and zigzag directions, respectively. By changing the lattice constants, we apply strain ranging from -0.02 to 0.02 along each directions, with steps of

0.01. Thus a data grid with 25 points is obtained. At each point we relax the internal atomic position, and calculate the strain energy E_s. The strain energy can be fitted by the formula $E_s = c_1{\varepsilon_x}^2 + c_2{\varepsilon_y}^2 + c_3\varepsilon_x\varepsilon_y$, in which ε_x and ε_y are the strain along x and y directions, respectively. The in-plane stiffness along x and y directions can then be calculated as $C_x = (1/S_0)(2c_1 - {c_3}^2/2c_2)$ and $C_y = (1/S_0)(2c_2 - {c_3}^2/2c_1)$. The Poisson's ratio along x and y directions can be obtained from $\nu_x = c_3/2c_2$ and $\nu_y = c_3/2c_1$. For structures with hexagonal symmetry, $c_1 = c_2$ in the harmonic region. Therefore, along x and y directions, the in-plane stiffness and Poisson's ratio of MoS_2 and HfS_2 are the same. On the other hand, TiS_3 exhibits anisotropic C and ν.

In-plane stiffness of MoS_2 is calculated to be 124.24 N/m, which is in good agreement with previously reported theoretical result of 138.12 N/m[13]. In addition, recently reported experimental in-plane stiffness value 180±60 N/m[19] also agrees with our result. Moreover one can deduce the effective Young's modulus from C/h by estimating the proper thickness h of the monolayer. Taking h=6.145 Å, which is the distance between the centers of two adjacent monolayers in bulk MoS_2, the Young's modulus of single layer MoS_2 can be determined as 202.18 GPa. In Ref.[19], the Young's modulus was calculated to be 270±100 GPa, corresponding to an effective thickness of 6.67 Å, which is close to our estimated value. In another experiment, the Young's modulus of few-layer MoS_2 was determined to be 330±70 GPa,[37] which is larger than our result. One reason for the difference can be explained by the difference in defining the effective thickness and the extra rigidity in a few-layered structure due to the layer-layer interaction. Given the facts that the distance between the two S layers in 2D MoS_2 is 3.13 Å and the effective thickness of monolayer MoS_2 would be larger than this value, the upper limit of the Young's modulus of monolayer MoS_2 can be estimated to be about 400 GPa, which is in line with the experimental value. The Poisson's ratio of MoS_2 is calculated to be 0.25.

Following the same methodology the in-plane stiffness of HfS_2 is found to be 79.86 N/m. Assuming an effective thickness equals to the bulk interlayer spacing 5.837 Å, the Young's modulus is 136.82 GPa. The calculated Poisson's ratio is 0.19, which is in agreement with a previous study[40].

Due to the anisotropic nature of TiS_3, its in-plane stiffness values are different in the x and y directions. We found C_x=83.33 N/m and C_y=133.56 N/m, in agreement with other calculations[20]. According to Ref.[38], the spacing between the centers of two adjacent layers in bulk TiS_3 is 8.706 Å. So the effective Young's modulus are 95.72 GPa and 153.41 GPa along the x and y, respectively. The Poisson's ratios are ν_x=0.11 and ν_y=0.18.

Our calculations reveal that in-plane stiffness values of these structures follow the trend $TiS_3(y) > MoS_2 > TiS_3(x) > HfS_2$. This trend can be understood in view of the bond length and the bond density in the different materials. A smaller bond length (thus a stronger bond) and a higher bond density per unit area would lead to a larger in-plane stiffness. In MoS_2 and HfS_2, the metal-sulfur bond length is 2.41 Å and 2.55 Å, respectively. In TiS_3, there are three different types of bonds. Along the y direction there are two types, with bond lengths of 2.46 Å and 2.50 Å. The third type is along the x direction, with bond length of 2.67 Å. The order of bond length is $TiS_3(x)$ >HfS_2 >$TiS_3(y)$ >MoS_2. Hence, the in-plane stiffness of MoS_2 and $TiS_3(y)$ is larger than that of $TiS_3(x)$ and HfS_2, due to the stronger chemical bonds. However only the bond lengths by themselves cannot explain the trend of the rigidity of those crystal structures. On the other hand, in TiS_3, each Ti is eight-fold coordinated, whereas the metal atoms are six-fold coordinated in the other two materials. In addition, the density of Ti per unit area is larger than that of Mo and Hf. As a result, the bond density in TiS_3 is higher than those of MoS_2 and HfS_2. When the bond strength is comparable, TiS_3 would have a larger in-plane stiffness because of the larger number of bonds. Thus the in-plane stiffness of $TiS_3(y)$ ($TiS_3(x)$) is larger than that of MoS_2 (HfS_2).

4.2 Ultimate Strength

In this part we discuss the strain-stress relation of MoS_2, TiS_3 and HfS_2. Using rectangular unit cells shown in Fig. 2 uniaxial strain is applied along x or y direction, and the cell vector perpendicular to the strain, as well as the atom positions, are fully relaxed. In many cases, nano-structure materials undergo reconstructions when applied strain is large enough. To explore possible reconstructions, in our calculations we break the imposed symmetry of the monolayers during the structural relaxation by randomly displacing a specified atom from its high symmetric position. If there is no reconstruction, the atom will go back after relaxation, and the original symmetry is preserved. Using the effective thickness of the monolayers mentioned above, the stress along the strain direction can be obtained after structural optimization. With increasing strain, the stress will increase first, and then reach a maximum, called the critical strain value, which corresponds to the ultimate strength of the monolayer. When the strain exceeds the critical value, the structure becomes unstable. In Fig. 2 the stress and strain energy of MoS_2, HfS_2 and TiS_3 are plotted as function of the applied strain.

With strain the symmetry of MoS_2 is lowered from D_{3h} to C_{2v}, therefore the mechanical response of MoS_2 becomes anisotropic for larger strain. When strain is along x, the maximum stress of 23.48 GPa is achieved at ε_x=0.26. This is in good agreement with the 27.35 GPa at ε_x=0.28 in Ref.[21] and the 24 GPa at ε_x=0.256 in Ref.[22]. Notice that when ε_x exceeds 0.26, there is a drop in the stress and strain energy, indicating a structural reconstruction of the monolayer. Indeed we find that the C_{2v} symmetry is no longer preserved when ε_x exceeds 0.26. The structural deformation is non-reversible in this region. This means that even when the applied strain is removed, the MoS_2 monolayer cannot relax to its equilibrium state as there is a energy barrier need to be overcome. This was not observed in previous studies[21,22], which probably results from the imposed symmetry when doing structural relaxation in those works. With strain along y direction, the ultimate strength of MoS_2 is found to be 15.99 GPa at ε_y=0.20, and agrees with 16.9 GPa at ε_y=0.19 in Ref.[21] and 15.6 GPa at ε_y=0.18 in Ref.[22]. We observe no reconstructions up to ε_y=0.26. The ultimate strength along the x and y directions shows obvious differences. The anisotropy can be measured by $\phi = \sigma_x/\sigma_y$, where σ_x and σ_y are the ultimate strength along x and y directions, re-

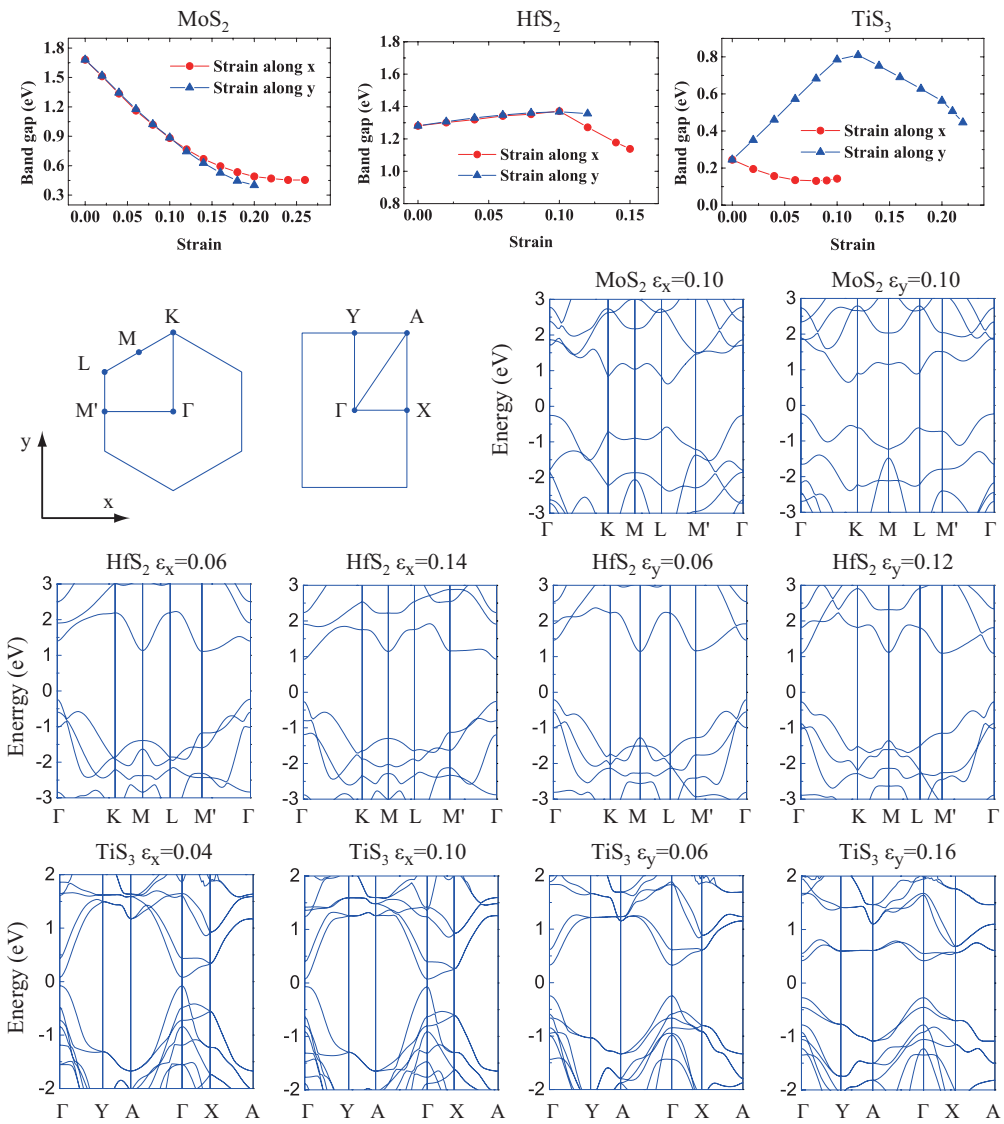

Fig. 3 (color online) The variation of the band gap of MoS_2, HfS_2 and TiS_3 with strain, and the band structure in the presence of different strain. The corresponding Brillouin zones and high symmetry k-paths are also shown.

spectively. For MoS_2 we found ϕ=1.47.

For HfS_2, the ultimate strength and strain along x are 14.16 GPa and 0.15, respectively. Along y direction, these values are 12.38 GPa and 0.13. The anisotropy factor of the ultimate strength is ϕ=1.14. Compared with 1H MoS_2, the anisotropy in 1T HfS_2 is smaller. Reconstructions occur beyond the ultimate strain, breaking the C_{2h} symmetry. The reconstructions with strain along x is non-reversible, as also proven by a decrease in strain energy. However, when strain is along y, we find that the deformation is minor between the reconstructed and unreconstructed structures. Therefore, the strain energy continues to grow when strain is larger than 0.13, suggesting a reversible reconstruction. Once the strain is released, the monolayer may return to the structure at $\varepsilon = 0$.

In TiS_3 monolayer, for strain along x, the ultimate strength is 4.45 GPa, with an ultimate strain of 0.10. When strain is along y, the ultimate strength and strain are 18.32 GPa and 0.22, respectively. In both cases, when the strain increases beyond the ultimate strains, the monolayer undergoes non-reversible structural reconstructions which break the original C_{2h} symmetry, as indicated by a sudden reduction in the strain energy and stress. The ultimate strength along x is much smaller than that along y, with an anisotropy factor of ϕ=0.24. This can be attributed to the anisotropy in the structure of TiS_3. As mentioned above, the bond length of TiS_3 along x direction is much larger as compared to the y direction. Therefore, the bond along x is weaker and easier to be broken, leading to a small ultimate strength and strain.

4.3 Modification of Electronic Structure with Strain

Finally, we investigate how the band structure is modified by the applied strain. Here, we especially focus on the strain range in which no reconstruction happens. For MoS_2 and HfS_2, we use the primitive unit cell to calculate the band structure instead of the rectangle unit cell. Note that the Brillouin zones of strained MoS_2 and HfS_2 are no longer hexagonal. In the strained cases, we adopt the notion of Ref.[39] to label the high-symmetrical k-points. At each strain value, we re-calculated the coordination of these points according to the deformed Brillouin zones. The variation of the band gap and the band structure of the different monolayers with uniaxial strain, are shown in Fig 3. For MoS_2, the band gap monotonously decreases when the strain increases, consistent with previous studies[39]. When strain is less than 0.1, the effects of x-strain and y-strain on the band gap are almost the same. Beyond this value, the gap decreases in the y-strain case is slightly faster than in the x-strain case. When strain along x becomes larger than 0.2, the gap saturates to 0.45 eV. Moreover, strain modifies the band edge position of MoS_2. Without strain MoS_2 has a direct band gap at the K and L points. When strain is applied, the band gap becomes indirect. The CBM state is located along the L-M′ for strain along x, and along K-Γ for strain along y. Under small strain, the CBM is close to the L or K symmetry point. As the strain increases, the CBM moves towards M′ or Γ. The VBM transfers to the Γ point with strain along both x and y. These observations are consistent with previous study[39].

In the case of HfS_2, without strain the monolayer is an indirect gap semiconductor with CBM at M (M′) and VBM at Γ. When the x-strain is smaller than 0.1, the CBM is at M′ and the VBM is at the Γ point. The gap value slightly increases with increasing strain, as shown in Fig. 3. When the x-strain is larger than 0.1, the CBM moves to the Γ point, while the VBM is still at Γ, leading to an indirect-to-direct gap transition. Because of the change of the CBM character, the band gap now decreases with increasing x-strain. In the y-strain case, the VBM is also found at the Γ point in the whole range considered. When ε_y is smaller than 0.08, the CBM is at M. At ε_y=0.1, the CBM changes to the M′ point. At ε_y=0.12, the CBM is located at the Γ point, and an indirect-to-direct gap transition occurs. The variation of the gap value with $\varepsilon_y < 0.1$ is very similar to that in the x-strain case. It is slightly larger with larger strain. From ε_y=0.1 to 0.12, the gap decreases a little. The origin is again the change of the CBM, as in the x-strain case. Overall, the anisotropy in the variation of the band gap with strain in HfS_2 is also small, especially in the small-strain range, similar to the case of MoS_2. The strain-induced indirect to direct gap transition is interesting for possible applications of HfS_2 in optoelectronics.

Compared with MoS_2 and HfS_2, the response of the band structure to strain in TiS_3 is very different. In the strained structures, the CBM and VBM states remain at the Γ point. Furthermore, it shows a strong anisotropy, as seen in Fig. 3. With increasing x-strain, overall the band gap shows a decreasing trend, and the magnitude is not large. From $\varepsilon_x = 0$ to $\varepsilon_x = 0.1$, the band gap reduction is about 0.1 eV. In case of y-strain, as the strain increases, the band gap becomes larger at first, and reaches 0.81 eV at $\varepsilon_y = 0.12$. When strain further increases, the band gap become smaller. To explore the origin of such a non-monotonous behavior, we look into the orbital character of the CBM and VBM states. We find that the CBM state of TiS_3 is formed by the d_{z^2} orbitals of the Ti atoms, and this character doesn't change with strain. The effect of strain on the CBM energy is also found to be small. However, the situation of the VBM is different. When ε_y is smaller than 0.12, the VBM state consists of the d_{xz} orbitals of the Ti atoms and the p_x orbitals of the four-fold coordinated S atoms in the interior. Whereas when ε_y is larger than 0.12, the dominant orbitals of the VBM state are the d_{xz} orbitals of the Ti atoms and the p_x orbitals of the two-fold coordinated S atoms on the surface. Due to the different orbital character, the response of the VBM state to strain is different in these two cases. For $\varepsilon_y < 0.12$, the VBM energy decreases as strain increases. When $\varepsilon_y > 0.12$, the VBM energy increases with increasing strain. Therefore, the band gap increases at first, and then decreases.

5 Conclusions

In summary, we have studied the mechanical properties of single layer transition-metal sulphides of three different structures MoS_2, HfS_2 and TiS_3. Our results reveal that the atomic coordination and crystal symmetry in these single layer crystal structures have a large influence on the mechanical properties. MoS_2 and HfS_2 have isotropic elastic parameters such as in-plane stiffness and Poisson's ratio, whereas those for TiS_3 are highly anisotropic. The ultimate mechanical strength for the three materials was also calculated. HfS_2 which is in the 1T phase has the smallest

anisotropy for the ultimate strength, whereas TiS_3 which is in the monoclinic phase has the largest. The band structure of these materials can be effectively tuned by uniaxial strain. Along both x and y directions, the band gap of MoS_2 decreases as strain increases, and the response is almost isotropic. Strong anisotropy is observed for TiS_3. The band gap decreases when strain is along x and increases when it is along y. However, when the strain along y reaches a threshold value, with further increasing strain the band gap reduces. For HfS_2, when strain is smaller (larger) than 0.1, the band gap increases (decreases), regardless of the strain direction. The recently synthesized TiS_3 showed extraordinary photoresponse which is promising for potential applications. HfS_2 is predicted to be a stable two-dimensional material and likely to be synthesized in the near future. Our results thus provide valuable information on the mechanical properties and electronic modifications when strain is applied. Also, the different characteristics observed in the sulphides with different structures shed light on the relationship between structure and properties, which are useful for their application.

6 Acknowledgement

This work was supported by the Flemish Science Foundation (FWO-Vl) and the Methusalem foundation of the Flemish government. Computational resources were provided by TUBITAK ULAKBIM, High Performance and Grid Computing Center (TR-Grid e-Infrastructure), and HPC infrastructure of the University of Antwerp (CalcUA) a division of the Flemish Supercomputer Center (VSC), which is funded by the Hercules foundation. H.S. is supported by a FWO Pegasus-Long Marie Curie Fellowship, and J.K. by a FWO Pegasus-Short Marie Curie Fellowship.

References

1 F. Hulliger, Struct. Bonding (Berlin), 1967, **4**, 83.
2 D. W. Bruce, *Transition Metal Sulphides: Chemistry and Catalysis*, eds. T. Weber, R. Prins and R. A. van Santen , (Kluwer Academic Publishers, Dordrecht, 1998).
3 W. A. Pryor, *Inorganic Sulphur Chemistry*. Ed. G. Nickless, (Elsevier, New York, 1968).
4 J. M. Hensen, V. H. J. De Beer, and R. A. Van Santen: *Chemistry and Reactivity of Transition Metal Sulphides in Relation to Their Catalytic Performance, Transition Metal Sulphides*, NATO ASI Series Volume 60, pp 169-188. (Springer, Netherlands, 1998).
5 J. Feng, X. Qian, C.-W. Huang, and J. Li, *Nature Photonics*, 2012, **6**, 866.
6 X. Hong, J. Kim, S.-F. Shi, Y. Zhang, C. Jin, Y. Sun, S. Tongay, J. Wu, Y. Zhang, and F. Wang, *Nature Nanotechnology*, 2014, **9**, 682.
7 M. Chhowalla, H. S. Shin, G. Eda, L.-J. Li, K. Ping Loh, and H. Zhang, *Nature Chemistry*, 2013, **5**, 263.
8 K. S. Novoselov, D. Jiang, F. Schedin, T. J. Booth, V. V. Khotkevich, S. V. Morozov, and A. K. Geim, *PNAS*, 2005, **102** 10451.
9 K. F. Mak, C. Lee, J. Hone, J. Shan, and T. F. Heinz, *Phys. Rev. Lett.*, 2010, **105**, 136805.
10 S. Bertolazzi, J. Brivio, and A. Kis, *ACS Nano*, 2011, **5**, 9703.
11 H. S. S. R. Matte, A. Gomathi, A. K. Manna, D. J. Late, R. Datta, S. K. Pati, and C. N. R. Rao, *Angew. Chem.*, 2010, **122**, 4153.
12 H. Q. Wang, K. Kalantar-Zadeh, A. Kis, J. N. Coleman, and M. S. Strano, *Nature Nanotech.*, 2012, **7**, 699.
13 C. Ataca, H. Sahin, and S. Ciraci, *J. Chem. Phys. C*, 2012, **116**, 8983.
14 J. Feng, L. Peng, C. Wu, X. Sun, S. Hu, C. Lin, J. Dai, J. Yang, and Y. Xie, *Adv. Mater.*, 2012, **24**, 1969.
15 C. Kreis, S. Werth, R. Adelung, L. Kipp, M. Skibowski, E. E. Krasovskii, and W. Schattke, *Phys. Rev. B*, 2003, **68**, 235331.
16 J. O. Island, M. Buscema, M. Barawi, J. M. Clamagirand, J. R. Ares, C. Sáchez, I. J. Ferrer, G. A. Steele, H. S. J. van der Zant, and A. Castellanos-Gomez, *Adv. Optic. Mater.*, 2014, **2**, 641.
17 F. Iyikanat, H. Sahin, R. T. Senger, and F. M. Peeters, *J. Phys Chem C*, 2015, **119**, 10709.
18 M. Topsakal, S. Cahangirov, and S. Ciraci, *Appl. Phys. Lett.*, 2010, **96**, 091912.
19 S. Bertolazzi, J. Brivio, and A. Kis, *ACS Nano*, 2011, **5**, 9703.
20 J. Dai and X. C. Zeng, arXiv:1501.02313.
21 J. Li, N. V. Medhekar, and V. B. Shenoy, *J. Chem. Phys. C*, 2013, **117**, 15842.
22 T. Li, *Phys. Rev. B*, 2014, **90**, 167402.
23 G. Kresse and J. Hafner, *Phys. Rev. B*, 1993, **47**, 558.
24 G. Kresse and J. Furthmüller, *Phys. Rev. B*, 1996, **54**, 11169.
25 P. E. Blöchl, *Phys. Rev. B*, 1994, **50**, 17953.
26 J. P. Perdew, K. Burke, and M. Ernzerhof, *Phys. Rev. Lett.*, 1996, **77**, 3865.
27 J. Heyd, G. E. Scuseria, and M. Ernzerhof, *J. Chem. Phys.*, 2003, **118**, 8207.
28 A. V. Krukau, O. A. Vydrov, A. F. Izmaylov, and G. E. Scuseria, *J. Chem. Phys.*, 2006, **125**, 224106.
29 H. J. Monkhorst and J. D. Pack, *Phys. Rev. B*, 1976, **13**, 5188.
30 D. Alfe, *Comput. Phys. Commun.*, 2009, **180**, 2622.
31 Y. Cai, J. Lan, G. Zhang, and Y.-W. Zhang, *Phys. Rev. B*, 2014, **89**, 035438.
32 Y. Cai, Q. Ke, G. Zhang, Y. P. Feng, V. B. Shenoy, and Y.-W. Zhang, *Adv. Funct. Mater.*, 2015, **25**, 2230.
33 R. Fei and L. Yang, *Appl. Phys. Lett.*, 2014, **105**, 083120.
34 T.J. Wieting, A. Grisel, and F. Lévy, *Physica B+C*, 1981, **105**, 366.
35 A. Molina-Sánchez and L. Wirtz, *Phys. Rev. B*, 2011, **84**, 155413.
36 Y. Li, Y. Rao, K. F. Mak, Y. You, S. Wang, C. R. Dean, and T. F. Heinz, *Nano Lett.*, 2013, **13**, 3329.
37 A. Castellanos-Gomez, M. Poot, G. A. Steele, H. S. J. van der Zant, N. Agraĺýt, and G. Rubio-Bollinger, *Adv. Mater.*, 2012, **24**, 772.
38 L. Brattas and A. Kjekshus, *Acta Chem. Scand.*, 1972, **26**, 3441.
39 P. Johari and V. B. Shenoy, *ACS Nano*, 2012, **6**, 5449.
40 D. M. Guzman and A. Strachan, *J. Appl. Phys.*, 2014, **115**, 243701.

41 J. Wu, D. Wang, H. Liu, W.-M. Lau, and L.-M. Liu, *RSC Adv.*, 2015, **5**, 21455.
42 A. Castellanos-Gomez, R. Roldán, E. Cappelluti, M. Buscema, F. Guinea, H. S. J. van der Zant, and G. A. Steele, *Nano Lett.*, 2013, **13**, 5361.
43 K. He, C. Poole, K. F. Mak, and J. Shan, *Nano Lett.*, 2013, **13**, 2931.
44 W. S. Yun, S. W. Han, S. C. Hong, I. G. Kim, and J. D. Lee, *Phys. Rev. B*, 2012, **85**, 033305.
45 E. Scalise, M. Houssa, G. Pourtois, V. Afanasąŕev, and A. Stesmans, *Nano Res.*, 2012, **5**, 43.